

Original Article

Cite this article: Liu B, Tang Y-J, Xing L-Y, Xu Y, Zhao S-Q, Sun Y, and Huang J (2022) Triassic calc-alkaline lamprophyre dykes from the North Qiangtang, central Tibetan Plateau: evidence for a subduction-modified lithospheric mantle. *Geological Magazine* **159**: 407–420. <https://doi.org/10.1017/S001675682100100X>

Received: 6 April 2021

Revised: 18 July 2021

Accepted: 14 September 2021

First published online: 24 November 2021

Keywords:



primitive magma; calc-alkaline lamprophyre; lithospheric mantle; slab rollback; Palaeo-Tethys

Author for correspondence:

Bin Liu,

Email: binliu@yangtzeu.edu.cn

Triassic calc-alkaline lamprophyre dykes from the North Qiangtang, central Tibetan Plateau: evidence for a subduction-modified lithospheric mantle

Bin Liu^{1,2} , You-Jun Tang³, Lü-Ya Xing³ , Yu Xu^{1,2}, Shao-Qing Zhao^{2,4}, Yang Sun^{1,2} and Jian Huang⁴

¹School of Geosciences, Yangtze University, Daxue Road 111, Wuhan 430100, China; ²State Key Laboratory of Petroleum Resources and Prospecting, China University of Petroleum, Fuxue Road 18, Beijing 102249, China; ³College of Resources and Environment, Yangtze University, Daxue Road 111, Wuhan 430100, China and ⁴State Key Laboratory of Geological Processes and Mineral Resources, China University of Geosciences, Lumo Road 388, Wuhan 430074, China

Abstract

Primitive lamprophyres in orogenic belts can provide crucial insights into the nature of the subcontinental lithosphere and the relevant deep crust–mantle interactions. This paper reports a suite of relatively primitive lamprophyre dykes from the North Qiangtang, central Tibetan Plateau. Zircon U–Pb ages of the lamprophyre dykes range from 214 Ma to 218 Ma, with a weighted mean age of 216 ± 1 Ma. Most of the lamprophyre samples are similar in geochemical compositions to typical primitive magmas (e.g. high MgO contents, Mg no. values and Cr, with low FeO_t/MgO ratios), although they might have experienced a slightly low degree of olivine crystallization, and they show arc-like trace-element patterns and enriched Sr–Nd isotopic composition ($(^{87}\text{Sr}/^{86}\text{Sr})_i = 0.70538\text{--}0.70540$, $\epsilon_{\text{Nd}}(t) = -2.96$ to -1.65). Those geochemical and isotopic variations indicate that the lamprophyre dykes originated from partial melting of a phlogopite- and spinel-bearing peridotite mantle modified by subduction-related aqueous fluids. Combining with the other regional studies, we propose that slab subduction might have occurred during Late Triassic time, and the rollback of the oceanic lithosphere induced the lamprophyre magmatism in the central Tibetan Plateau.

1. Introduction

Calc-alkaline lamprophyres are a unique rock type of volatile-rich (such as H₂O and CO₂) hypabyssal rocks, which are typically emplaced as a small volume of dykes, sills and plugs (Rock, 1991). Moreover, they are generally featured by a diagnostic porphyritic texture with plentiful idiomorphic phenocrysts of hornblende and/or biotite. Lamprophyres have attracted much attention during the last few decades as a result of their unusual mineralogy and an apparent uncoupling of geochemical compositions as mantle- and crust-derived melts (Abdelfadil *et al.* 2013). Moreover, lamprophyres are widely considered to mark the thermal and compositional fingerprints of the lithosphere (Karsli *et al.* 2014; Ma *et al.* 2014), and their generation had been attributed to a variety of the continental-scale geodynamic processes such as slab subduction and post-collisional and intraplate rifting (Aghazadeh *et al.* 2015). Identifying those primitive lamprophyres from the orogenic belts could not only provide crucial insights into the nature of the subcontinental lithosphere and the interactions between the deep mantle and diversified crustal materials, but also can aid in understanding the geodynamic history of ancient convergent margins.

Most of the mafic magmas (including the lamprophyre melts) from the orogenic belts usually experienced a complex evolution involving fractionation and crustal contamination during migration through the crust, which might make attempts to reveal their mantle source and generation difficult (Rogers & Hawkesworth, 1989; Halama *et al.* 2004). In contrast, the primitive or relatively primitive magmas underwent only minimal fractionation or crustal contamination since leaving the mantle sources, and can therefore provide a more sensitive probe of the mantle source (Leat *et al.* 2002). The primitive magmas are usually characterized by relatively low FeO_t/MgO (< 1), and high Mg no. ($= 100 \times \text{Mg}^{2+}/(\text{Mg}^{2+} + \text{Fe}_t^{2+})$; > 64), Ni (> 200 ppm) and Cr (> 400 ppm; Tatsumi & Eggins, 1995). Although the primitive magmas are volumetrically minor on earth, they are often exposed in the many arcs such as the Marianas, South Sandwich and Cascade arcs (Leat *et al.* 2002; Mullen *et al.* 2017). The central Tibetan Plateau is a key area for comprehending the Palaeo-Tethyan tectonic evolution because of the preservation of many ophiolites or sutures, and abundant Triassic high-pressure (HP) to ultra-high-pressure

(UHP) metamorphic rocks. However, the genetic mechanism of the widespread Upper Triassic magmatic rocks has long been a subject of debate. Many previous studies had been conducted on the granitoid rocks and intermediate to acid volcanic rocks, and proposed two competing mechanisms including a subduction-related model and a collision-related model for the generation of the Late Triassic magmatism (Zhang *et al.* 2007, 2014; Peng *et al.* 2015; Liu *et al.* 2016a; Yang *et al.* 2020). Although some Middle Triassic mafic rocks have been reported in the central Tibetan Plateau (Liu *et al.* 2020), the mantle sources and petrogenesis of Upper Triassic mafic rocks remain unclear, limiting our knowledge of the lithospheric mantle and hindering our ability to decipher the Triassic tectonic evolution.

Through detailed investigations, we have recently identified a series of calc-alkaline lamprophyre dykes in the North Qiangtang terrane, central Tibetan Plateau, which have geochemical compositions comparable to those of typical primitive magmas from the modern arcs (Leat *et al.* 2002). In this study, we conducted a systematic analysis of the zircon U–Pb geochronology, mineral chemistry, bulk-rock geochemistry and Sr–Nd–Hf isotopic composition of the lamprophyre dykes. The data are used to constrain their mantle source, petrogenesis and geodynamic setting to enhance our understanding of the subcontinental lithospheric mantle, and to shed more light on the Late Triassic tectonic evolution of the central Tibetan Plateau.

2. Geological background and sample description

The Qiangtang terrane mainly consists of two parts, the South Qiangtang terrane (SQT) and the North Qiangtang terrane (NQT), which are separated by the central Qiangtang metamorphic belt (also referred to as the Longmuco–Shuanghu suture zone; Li *et al.* 2007). The NQT is bounded by the Longmuco–Shuanghu suture zone to the south and the Garzê–Litang suture zone to the north (Fig. 1a).

The Longmuco–Shuanghu suture zone is featured by the presence of many dismembered ophiolitic mélanges and high-pressure metamorphic rocks (e.g. Triassic eclogites and blueschists; Zhai *et al.* 2011; Dan *et al.* 2018). It has recently been considered as a main ocean of the Palaeo-Tethys in the central Tibetan Plateau (Metcalfe, 2013; Xu *et al.* 2015), although it had been previously interpreted as a tectonic mélange of the Songpan–Garzê flysch deposits underthrust along the Jinshajiang suture zone (Pullen *et al.* 2008). Geochronological studies on those metamorphic rocks have revealed that the timing of the eclogite-facies metamorphism is *c.* 233 Ma (Dan *et al.* 2018), while the timing of the exhumation of the eclogites is 222–203 Ma (Kapp *et al.* 2003; Dan *et al.* 2018). The Garzê–Litang suture zone also marks a northern branch of the Palaeo-Tethyan ocean, which might be initiated by the rollback of the Longmuco–Shuanghu oceanic lithosphere (Liu *et al.* 2016b, 2020). It is characterized by the exposure of voluminous Triassic ophiolitic mélanges with ages in the range 232–240 Ma. (Duan *et al.* 2009; Zhang *et al.* 2012; Liu *et al.* 2016b), although some Permian mafic complexes have also been discovered (Yan *et al.* 2005). Those Triassic ophiolitic mélanges are dominated by pillow basalts, gabbros, diabases and some altered peridotites. The mafic complexes usually display BABB-type or OIB-type affinities (Liu *et al.* 2016b), and they are similar in mineral and geochemical compositions to the Triassic mafic rocks in the NQT (Liu *et al.* 2020).

The SQT is predominantly composed of Cambrian–Silurian and Carboniferous–Jurassic sedimentary sequences. The discovery of the Carboniferous–Permian cold-water biota and glaci-marine

deposits indicates that the SQT has a Gondwana affinity (e.g. Li *et al.* 2007). Early Permian radial mafic dyke swarms and flood basalts developed in the SQT, and are usually considered as the results of a mantle plume activity in northern Gondwana during Sakmarian–Kungurian time (Zhang & Zhang, 2017). The NQT is covered by Devonian–Permian and Triassic–Cenozoic sedimentary rocks. Because the Carboniferous–Permian sedimentary units have many warm-water fossils (Metcalfe, 2013; Xu *et al.* 2020), the NQT might have a Cathaysian affinity rather than a Gondwanan affinity. Recent studies have documented the Proterozoic Ningduo metamorphic rocks (991–1044 Ma; He *et al.* 2013) and the oldest detrital zircons of *c.* 4.0 Ga (He *et al.* 2011), suggesting that a Precambrian crystalline basement developed beneath the NQT. Permian–Lower Triassic volcanic rocks and granitoids are widespread in the NQT, especially in the Tuotuohe to Yushu area. Most of them exhibit arc-like composition, which could be due to the northwards subduction of the Longmuco–Shuanghu ocean (Yang *et al.* 2011). Additionally, the rollback of the oceanic lithosphere, combined with the activity of the Emeishan mantle plume, triggered a series of Permian–Triassic mafic magmatism in the NQT (Liu *et al.* 2016a, 2020).

In this research, we have investigated a series of lamprophyre dykes in the north margin of the NQT (Fig. 1b). The lamprophyre dykes intrude the Longbao diorite pluton, which is emplaced into the Triassic low-grade metamorphosed clastic rocks of the Zhiduo–Yushu mélange. All the dykes exhibit sharp contacts with the host diorite pluton, and some dykes contain a small number of diorite xenoliths. They extend in an approximate NW–SE direction and their thicknesses range from 15 to 80 cm. The lamprophyre dykes show a characteristic lamprophyric texture in thin-sections (Fig. 2). The phenocrysts consist of plentiful idiomorphic hornblendes, while the matrixes are mainly composed of anhedral plagioclases and fine-grained hornblendes. The hornblende phenocrysts display an obvious pleochroism from brown to green and some of them have simple twinning. The plagioclases occur as interstitial mineral phases surrounding the idiomorphic hornblende phenocrysts, and the polysynthetic twinning can be found in some plagioclase with a relatively larger grain size.

3. Analytical methods

Zircon grains for the U–Pb isotopic dating were extracted using standard mechanical crushing, heavy magnetic-liquid techniques and handpicking. Cathodoluminescence (CL) images and transmitted to reflected light photomicrographs were used to check zircon textures and the related analytical sites. Zircon U–Pb isotopic analyses were performed using a GeoLas 2005 and an Agilent 7500a inductively coupled plasma mass spectrometer (ICP-MS) at the State Key Laboratory of Geological Processes and Mineral Resources (GPMP), China University of Geosciences (Wuhan). The spot size was 32 μm , while the frequency and energy of the laser were set to 6 Hz and *c.* 60 mJ, respectively. The 91500, NIST 610 and GJ-1 were applied as external standards for the elemental analyses and the isotopic normalizing. The operating conditions of the instruments and the offline-data calculation are described by Liu *et al.* (2008, 2010).

Bulk-rock major-element contents of six samples were carried out by measuring X-ray fluorescence (XRF; Primus II, Rigaku) at the Wuhan Sample Solution Analytical Technology Co., Ltd. For major elements, the analytical precision and accuracy of the two instruments were better than 5%. Bulk-rock concentrations of trace elements were tested using an Agilent 7500a ICP-MS

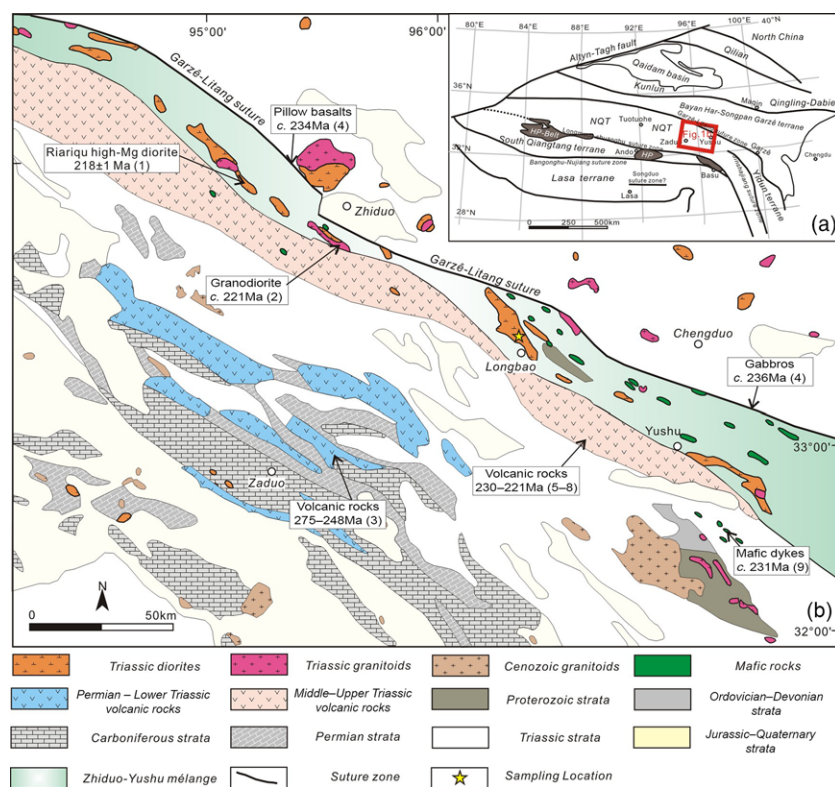


Fig. 1. (Colour online) (a) Location of the central Tibetan Plateau and (b) simplified geological map of the study area. Data sources for the zircon U–Pb ages are as follows: (1) Zhao *et al.* (2015); (2) Tan *et al.* (2019); (3) Yang *et al.* (2011); (4) Liu *et al.* (2016b); (5–8) Liu *et al.* (2016a), Liu *et al.* (2019), Zhao *et al.* (2014); (9) Liu *et al.* (2020).

instrument at the GPMR. Typical samples were digested in the Teflon bombs using HF + HNO₃. The analytical results of the standard materials (e.g. BCR-2, RGM-2, AGV-2 and BHVO-2) and the replicate samples are listed in the online Supplementary Material (available at <http://journals.cambridge.org/geo>). Bulk-rock Sr–Nd isotopic compositions of the representative samples were obtained at the GPMR using a Finnigan Triton thermal ionization mass spectrometer (TIMS) and a multi-collector (MC-) ICP-MS instrument. The TIMS and the MC-ICP-MS are applied to quantify the ratios of ⁸⁷Sr/⁸⁶Sr and ¹⁴³Nd/¹⁴⁴Nd, respectively. Detailed experimental methods are reported by Gao *et al.* (2004). The mass fractionation corrections of the isotopic ratios were conducted by using ¹⁴⁶Nd/¹⁴⁴Nd = 0.721900 and ⁸⁸Sr/⁸⁶Sr = 8.375209. Additionally, analyses made on the standard NBS 987 and JNdi-1 yielded the average ⁸⁸Sr/⁸⁶Sr ratio of 0.710274 ± 0.000009 and the average ¹⁴⁶Nd/¹⁴⁴Nd ratio of 0.512118 ± 0.000009, respectively.

4. Results

4.a. Zircon U–Pb ages

The sample JL01 for zircon U–Pb dating was collected from the site at 33° 17.006' N, 96° 24.977' E. Results of the LA-ICP-MS zircon U–Pb dating are given in Table 1, and plotted in Figure 3. The analytical sites and CL images of the representative zircon grains are also given in Figure 3.

The zircon grains are mostly colourless or fawn, transparent and with grain sizes ranging over 30–150 μm. LA-ICP-MS U–Pb isotopic analyses were performed on 25 zircon grains. Seven of these grains have subhedral to anhedral crystals, and show an obvious core–rim structure in the CL images. Those grains have relatively low Th/U ratios of 0.03–0.89, and yield relatively old and scattered ²⁰⁶Pb/²³⁸U ages of 234–1213 Ma, which could be explained as the ages of the old inherited zircons. The other 18

zircon grains exhibit euhedral columnar or tabular shapes, and most of them display pronounced broadly spaced oscillatory zoning without complicated internal textures in the CL images, which is the analogy to those of typical mafic magmatic zircons (e.g. Wang *et al.* 2013). Furthermore, those grains have relatively high Th/U ratios of 0.20–0.93. These features strongly argue that the other 18 zircon grains might be crystallized from the mafic magmas rather than inherited from the magma conduit. Analyses of those 18 grains give relatively uniform ²⁰⁶Pb/²³⁸U ages of 214–218 Ma, and define a weighted mean age of 216 ± 1 Ma with a mean square weighted deviation (MSWD) of 0.24. This mean age could be regarded as the crystallization time of the lamprophyre dykes in the NQT.

4.b. Major and trace elements

Analytical results of bulk-rock major and trace elements for the typical lamprophyre samples are given in Table 2.

The lamprophyre samples have moderate contents of SiO₂ (47.64–48.97 wt%), Al₂O₃ (13.74–15.69 wt%) and FeOt (8.54–9.14 wt%), low content of Na₂O + K₂O (3.66–4.16 wt%), and relatively high Na₂O/K₂O ratios of 1.28–1.82. They have relatively low TiO₂ contents of 1.09–1.14 wt%, which could be comparable to those of island-arc calc-alkaline basalts (c. 0.98 wt%; Pearce, 1982) and distinctly lower than those of within-plate tholeiitic basalts (c. 2.23 wt%; Pearce, 1982). All samples plot in the field of subalkaline basalts on the Zr/TiO₂ versus Nb/Y diagram (Fig. 4a), and they fall within the field of medium-K to high-K calc-alkaline lamprophyre on the K₂O versus SiO₂ diagram (Fig. 4b). Additionally, most of the samples have relatively high MgO contents (8.80–9.43 wt%), Mg no. (> 64) and Cr (> 400 ppm), with low FeOt/MgO ratios (< 1), analogous to those of the primitive magmas defined by Tatsumi & Eggins (1995).

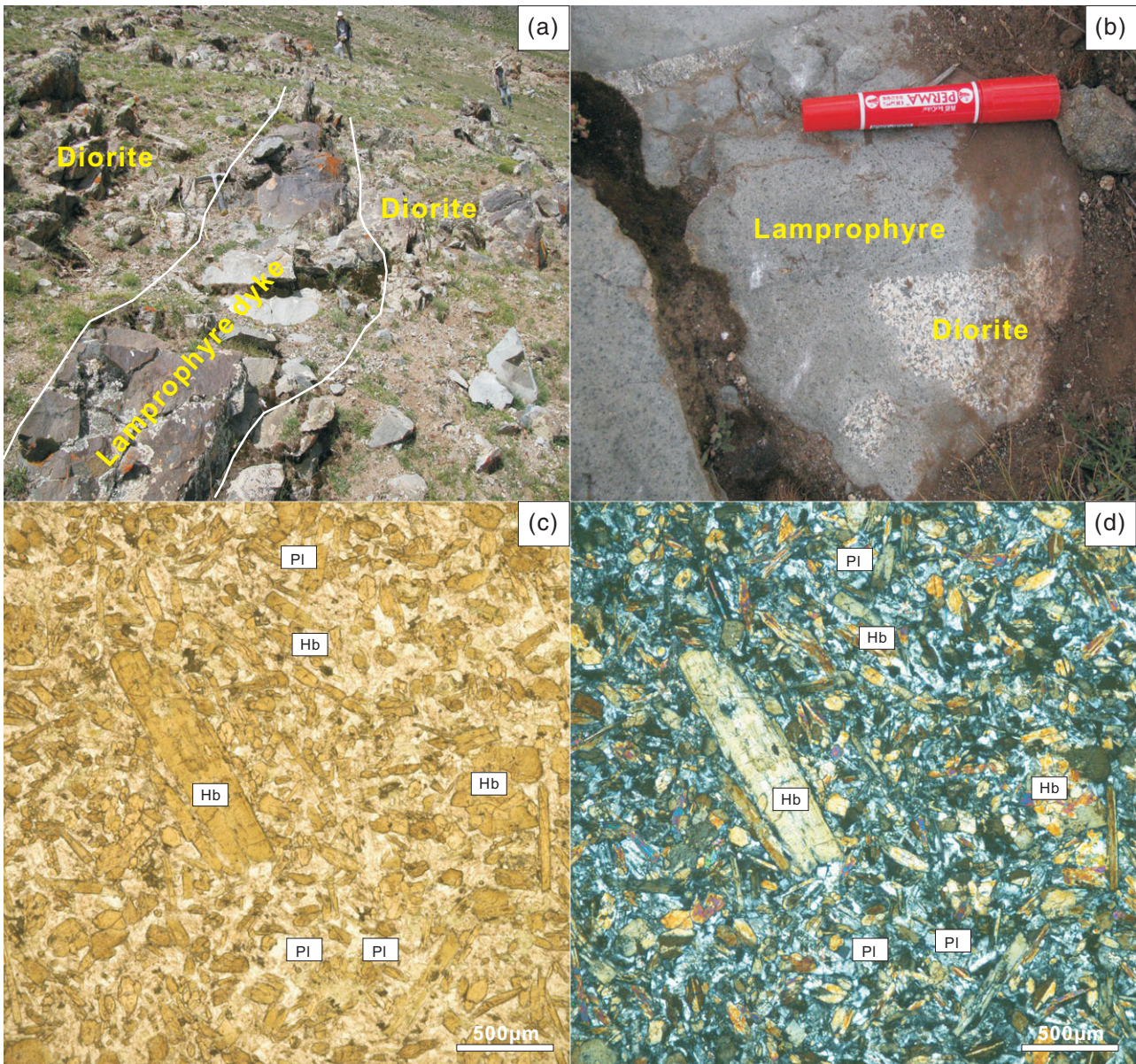


Fig. 2. (Colour online) (a–d) Photomicrographs of the Triassic lamprophyre dykes from the North Qiangtang terrane. Hb – hornblende; Pl – plagioclase.

The samples have comparatively high contents of rare earth elements (REEs), and their Σ REE values range over 99.83–121.29 ppm. All of them have comparatively high $(La/Yb)_N$ ratios of 5.96–7.23, and display an apparent enrichment of light REEs concerning heavy REEs on the chondrite-normalized REE patterns (Fig. 5a). Moreover, the samples have slightly negative Eu anomalies with Eu/Eu^* ratios of 0.92–0.99. On the primitive-mantle-normalized trace-element patterns (Fig. 5b), the samples are depleted in high-field-strength elements (such as Nb, Ta and Ti), and enriched in the light REEs and some large-ion lithophile elements (LILEs; e.g. Th). Such trace-element patterns are analogous to those of the primitive melts of subduction-modified lithospheric mantle in the Antarctic Peninsula (Leat *et al.* 2002).

4.c. Sr–Nd isotopic composition

Bulk-rock Sr–Nd isotopic composition and the calculated parameters of four typical lamprophyre samples are presented in Table 3,

and plotted in Figure 6. The initial values of Sr and Nd isotopic composition were calculated based on a timing of 215 Ma. The samples have relatively high initial $^{87}Sr/^{86}Sr$ ratios ($(^{87}Sr/^{86}Sr)_i$) of 0.70538–0.70540, and relatively low $\epsilon_{Nd}(t)$ values of –2.96 to –1.65. On the $\epsilon_{Nd}(t)$ versus $(^{87}Sr/^{86}Sr)_i$ diagram, the samples exhibit distinctly lower $\epsilon_{Nd}(t)$ values than those of the mafic rocks from the Triassic ophiolites in the Garzê–Litang suture zone.

5. Discussion

5.a. Effects of post-magmatic alterations

It is necessary to evaluate the effects of the post-magmatic alteration on the lamprophyre dykes, because most of the samples have comparatively high loss-on-ignition values (LOIs; 2.45–5.16 wt%). Considering that Zr has been proven to be one of the most stable elements during the medium- to low-grade metamorphism and alteration, the correlations between Zr and the

Table 1. Zircon LA-ICP-MS dating results for the Triassic lamprophyre dykes

Sample spots	Concentration (ppm)		Th/U	Isotopic ratios						Apparent ages (Ma)					
	²³² Th	²³⁸ U		²⁰⁷ Pb/ ²⁰⁶ Pb	±1σ	²⁰⁷ Pb/ ²³⁵ U	±1σ	²⁰⁶ Pb/ ²³⁸ U	±1σ	²⁰⁷ Pb/ ²⁰⁶ Pb	±1σ	²⁰⁷ Pb/ ²³⁵ U	±1σ	²⁰⁶ Pb/ ²³⁸ U	±1σ
JL01-01	350	395	0.89	0.05763	0.00561	0.29345	0.02824	0.03693	0.00053	516	221	261	22	234	3
JL01-02	74.2	1780	0.04	0.08569	0.00216	1.62453	0.03655	0.13750	0.00157	1331	50	980	14	831	9
JL01-03	200	320	0.62	0.04605	0.00377	0.24249	0.01957	0.03819	0.00052	–	180	220	16	242	3
JL01-04	159	361	0.44	0.04722	0.00237	0.22123	0.01056	0.03412	0.00054	60	76	203	9	216	3
JL01-05	248	1246	0.20	0.04921	0.00169	0.23297	0.00762	0.03421	0.00039	158	55	213	6	217	2
JL01-06	249	516	0.48	0.04940	0.00221	0.23004	0.01024	0.03372	0.00037	167	83	210	8	214	2
JL01-07	367	1248	0.29	0.05522	0.00476	0.29916	0.02555	0.03929	0.00049	421	197	266	20	248	3
JL01-08	210	531	0.40	0.05038	0.00298	0.23411	0.01356	0.03370	0.00040	213	137	214	11	214	2
JL01-09	25.3	787	0.03	0.09735	0.00245	2.77825	0.05795	0.20699	0.00292	1574	48	1350	16	1213	16
JL01-10	144	275	0.52	0.05507	0.01350	0.30160	0.07355	0.03972	0.00100	415	471	268	57	251	6
JL01-11	224	623	0.36	0.05120	0.00371	0.24385	0.01794	0.03438	0.00067	250	132	222	15	218	4
JL01-12	185	490	0.38	0.05922	0.00388	0.27445	0.01726	0.03391	0.00046	575	114	246	14	215	3
JL01-13	256	742	0.34	0.05179	0.00320	0.24222	0.01435	0.03434	0.00058	276	105	220	12	218	4
JL01-14	396	1008	0.39	0.04697	0.00236	0.21937	0.01043	0.03433	0.00046	48	78	201	9	218	3
JL01-15	264	657	0.40	0.05412	0.00290	0.24980	0.01309	0.03412	0.00054	376	89	226	11	216	3
JL01-16	259	514	0.50	0.04794	0.00314	0.22621	0.01519	0.03420	0.00055	96	119	207	13	217	3
JL01-17	494	1224	0.40	0.04741	0.00204	0.22261	0.00964	0.03404	0.00037	70	76	204	8	216	2
JL01-18	421	947	0.44	0.04748	0.00234	0.22102	0.01057	0.03421	0.00043	74	83	203	9	217	3
JL01-19	152	581	0.26	0.05060	0.00367	0.23416	0.01654	0.03402	0.00060	223	128	214	14	216	4
JL01-20	1516	1634	0.93	0.05262	0.00209	0.24566	0.00955	0.03401	0.00040	312	67	223	8	216	2
JL01-21	616	1131	0.54	0.05327	0.00241	0.30235	0.01466	0.04108	0.00070	340	79	268	11	260	4
JL01-22	395	970	0.41	0.05387	0.00267	0.25324	0.01270	0.03391	0.00046	366	89	229	10	215	3
JL01-23	247	717	0.34	0.05530	0.00277	0.25735	0.01280	0.03394	0.00046	424	87	233	10	215	3
JL01-24	255	721	0.35	0.05239	0.00303	0.24191	0.01348	0.03398	0.00056	303	97	220	11	215	3
JL01-25	369	902	0.41	0.05314	0.00253	0.24528	0.01129	0.03383	0.00050	335	77	223	9	214	3

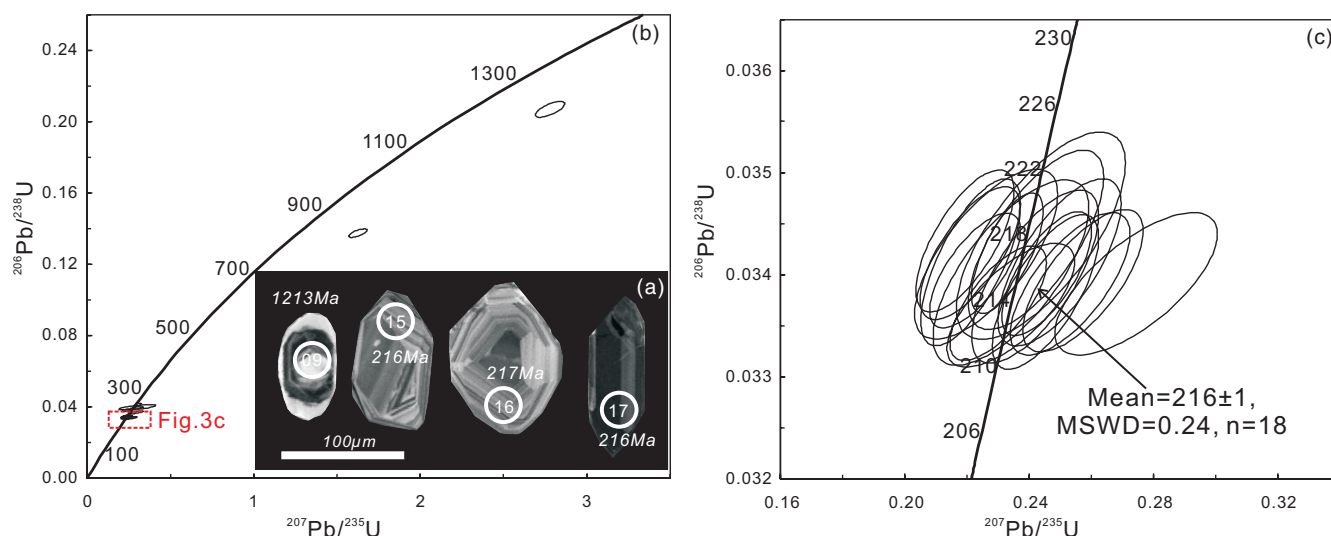
**Fig. 3.** (Colour online) (a–c) Zircon U–Pb Concordia plots with CL images of representative zircons for the Triassic lamprophyre dykes. The white circles in the CL images indicate analytical spots of the zircon U–Pb dating.

Table 2. Major- (in wt%), trace-element (ppm) and Sr–Nd isotopic compositions of the Triassic lamprophyre dykes

Sample no.	JL01-1	JL02-1	JL03-2	JL03-3	JL04-1	JL05-3
SiO ₂	48.73	48.67	48.59	48.97	48.59	47.64
TiO ₂	1.14	1.09	1.13	1.08	0.99	1.09
Al ₂ O ₃	15.43	14.89	15.13	15.69	13.74	14.66
Fe ₂ O ₃	2.21	2.71	2.49	2.35	9.49	9.94
FeO	6.95	6.70	6.80	6.50	–	–
FeO _t	8.94	9.14	9.04	8.61	8.54	8.95
MnO	0.19	0.19	0.19	0.18	0.17	0.19
MgO	9.26	9.44	9.44	9.05	8.80	8.26
CaO	9.25	9.05	8.61	8.65	8.38	9.43
Na ₂ O	2.36	2.44	2.18	2.46	2.33	2.36
K ₂ O	1.30	1.50	1.65	1.57	1.82	1.65
P ₂ O ₅	0.48	0.43	0.49	0.47	0.41	0.51
LOI	2.45	2.66	3.06	2.80	5.16	4.17
Mg no.	65	65	65	65	65	62
Sc	32.1	31.4	32.5	31.3	28.8	31.7
V	210	203	211	204	192	221
Cr	450.1	450.8	530.8	542.4	571.5	404.4
Co	49.3	48.9	52.3	53.2	35.9	37.0
Ni	128.4	130.4	145.4	135.8	152.1	123.4
Cu	93.4	24.2	42.8	58.8	17.7	20.8
Zn	77.1	78.2	79.2	74.2	77.9	85.7
Ga	18.1	17.7	18.4	17.3	16.0	19.2
Rb	59.3	77.6	75.5	77.4	68.9	69.0
Sr	545	506	554	514	381	546
Y	24.1	22.7	24.7	22.7	20.7	23.5
Zr	104	103	120.7	105.8	95	113
Nb	10.5	10.1	12.1	10.7	9.6	12.0
Cs	1.2	1.4	1.2	1.9	1.2	1.2
Ba	629	480	638	488	656	575
La	20.4	19.7	23.1	19.8	18.4	23.4
Ce	42.5	40.0	45.9	40.4	37.6	45.9
Pr	5.3	5.0	5.7	5.0	4.7	5.6
Nd	22.5	21.0	23.9	21.4	19.6	23.0
Sm	5.17	4.68	5.16	4.56	4.42	5.24
Eu	1.50	1.40	1.59	1.39	1.31	1.56
Gd	4.33	4.29	4.51	4.22	4.18	4.60
Tb	0.69	0.66	0.71	0.65	0.64	0.67
Dy	4.10	3.92	4.39	3.85	3.70	4.01
Ho	0.82	0.77	0.84	0.79	0.75	0.81
Er	2.25	2.16	2.36	2.14	2.03	2.29
Tm	0.33	0.31	0.37	0.31	0.30	0.33
Yb	2.27	2.23	2.38	2.16	1.88	2.18
Lu	0.34	0.33	0.37	0.34	0.31	0.37

(Continued)

Table 2. (Continued)

Sample no.	JL01-1	JL02-1	JL03-2	JL03-3	JL04-1	JL05-3
Hf	2.92	2.88	3.22	2.86	2.67	3.22
Ta	0.79	0.76	0.93	0.80	0.74	0.86
Pb	12.3	4.8	6.8	6.1	9.5	9.2
Th	9.46	9.15	11.02	9.80	8.80	10.83
U	2.87	3.31	3.91	2.98	3.02	3.85

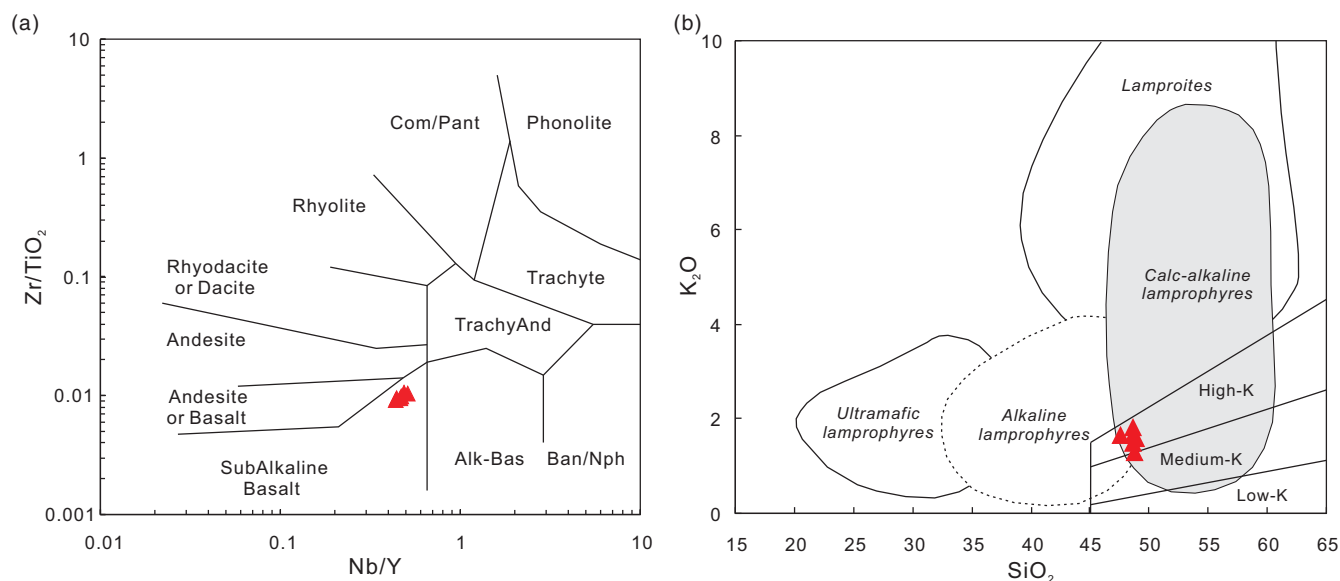
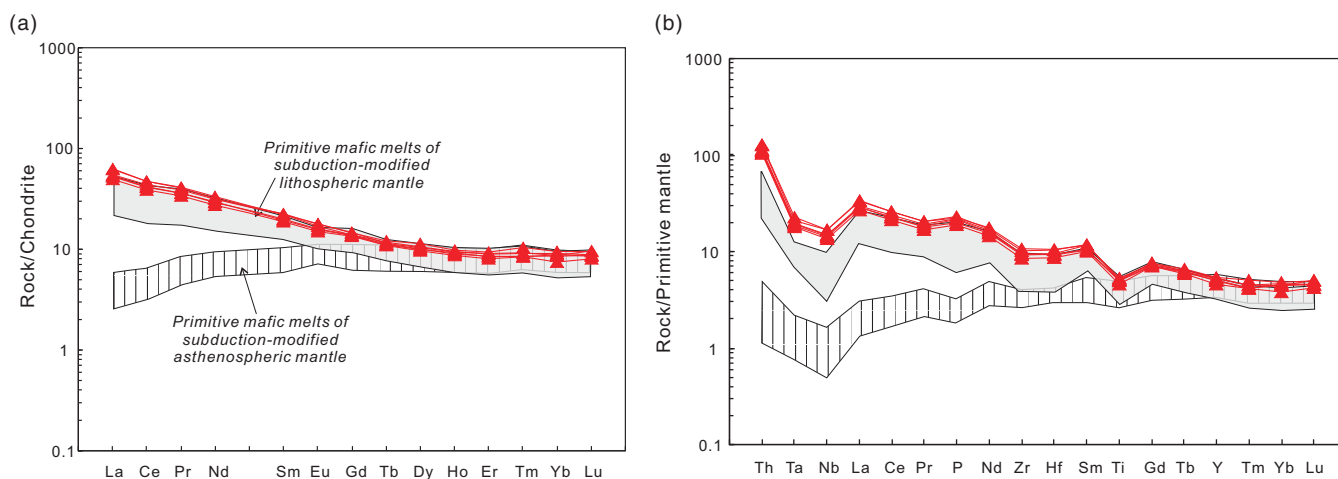
Fig. 4. (Colour online) Plots of (a) Zr/TiO_2 versus Nb/Y (Winchester & Floyd, 1977) and (b) K_2O versus SiO_2 (Rock, 1991) for the Triassic lamprophyre dykes.

Fig. 5. (Colour online) (a) Chondrite-normalized REE distribution patterns and (b) primitive-mantle-normalized trace-element spider diagrams for the Triassic lamprophyre dykes. Chondrite data from Taylor & McLennan (1985); primitive mantle data from Sun & McDonough (1989).

other elements have been widely used to assess the element mobility (Polat & Hofmann, 2003). In order to evaluate the alteration effects on various chemical compositions of the samples, representative major oxides (e.g. MgO , FeO , TiO_2 , P_2O_5 , K_2O and Na_2O) and trace elements (e.g. Rb, Ba, Sr, Cr, Ni, Eu, Nb, La, Ce, Th, Lu and Yb) were plotted against Zr. In the online

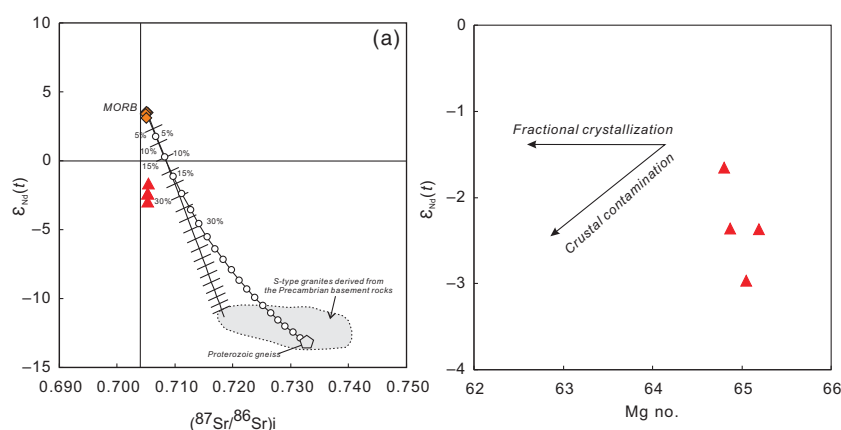
Supplementary Material, the above-listed elements are strongly or roughly correlated with Zr, and the LOIs do not form a correlation with Zr. In addition, all the samples show uniform REE and trace-element patterns. Such observations indicate that those above-listed elements were not affected by the alterations.

Table 3. Sr–Nd isotopic compositions of typical samples from the Triassic lamprophyre dykes

Sample no.	$^{87}\text{Rb}/^{86}\text{Sr}$	$^{87}\text{Sr}/^{86}\text{Sr}$	$\pm 2\sigma$	$^{147}\text{Sm}/^{144}\text{Nd}$	$^{143}\text{Nd}/^{144}\text{Nd}$	$\pm 2\sigma$	t (Ma)	$(^{87}\text{Sr}/^{86}\text{Sr})_i$	$\epsilon_{\text{Nd}}(t)$
JL01-1	0.314447	0.706364	5	0.139217	0.512436	5	215	0.70540	−2.36
JL02-1	0.443506	0.706782	7	0.134711	0.512466	4	215	0.70543	−1.65
JL03-2	0.393993	0.706590	6	0.130641	0.512393	6	215	0.70539	−2.97
JL03-3	0.435585	0.706733	6	0.128904	0.512421	5	215	0.70540	−2.37
JD-24h ^a	–	0.713077	6	–	0.512126	6	–	–	–
JD-24h ^a	–	0.713097	7	–	0.512126	3	–	–	–

^aReplicate analyses at the State Key Laboratory of Geological Processes and Mineral Resources (GPMR), China University of Geosciences (Wuhan).

Fig. 6. (Colour online) Plot of (a) $\epsilon_{\text{Nd}}(t)$ versus $(^{87}\text{Sr}/^{86}\text{Sr})_i$ and (b) $\epsilon_{\text{Nd}}(t)$ versus Mg no. for the Triassic lamprophyre dykes. Triassic S-type granites and Proterozoic gneiss (Tao *et al.* 2014; Peng *et al.* 2015) are shown for comparison. MORB data from Liu *et al.* (2016b). The MORB-type asthenosphere mantle is represented by: Nd = 12.7 ppm, Sr = 93.69 ppm, $^{87}\text{Sr}/^{86}\text{Sr} = 0.705372$ and $^{143}\text{Nd}/^{144}\text{Nd} = 0.512811$. Two typical types of crustal components are represented by (1) Nd = 20.9 ppm, Sr = 161 ppm, $^{87}\text{Sr}/^{86}\text{Sr} = 0.723624$ and $^{143}\text{Nd}/^{144}\text{Nd} = 0.511967$, and (2) Nd = 27.4 ppm, Sr = 105 ppm, $^{87}\text{Sr}/^{86}\text{Sr} = 0.740191$ and $^{143}\text{Nd}/^{144}\text{Nd} = 0.511865$.



5.b. Crustal contamination and differentiation

Before constraining the magma source characteristics of the lamprophyre dykes, it is necessary to access the possible influences of the crustal contamination and magma differentiation. Crustal contamination could observably change the geochemical and isotopic composition of mafic melts during magma ascent (DePaolo, 1981; Halama *et al.* 2004). In that case, P_2O_5 and TiO_2 contents and $\epsilon_{\text{Nd}}(t)$ values would decrease, while the abundances of LILEs, Na_2O and K_2O would increase. However, the TiO_2 and P_2O_5 contents of lamprophyre samples remain constant with decreasing Mg no. values, which are different from the features of the crustal contamination. The samples do not show a positive correlation between $\epsilon_{\text{Nd}}(t)$, Nb/La and Mg no. values (Figs 6, 7), also suggesting that the contamination seems to be negligible. Their ratios of Nb/Ce and Nb/La (0.25–0.26 and 0.51–0.54, respectively) are lower than those of the average crust, the lower crust and the primitive mantle, suggesting no significant crustal contamination. All samples exhibit markedly negative Zr and Hf anomalies relative to the primitive mantle, and have homogeneous Sr–Nd isotopic compositions with uniform trace-element patterns. The ordinary Sr–Nd isotopic model (Fig. 6) indicates that those rocks could not have originated from the mixing between mid-ocean-range basalt (MORB) and crustal components (represented by the Proterozoic gneiss and the S-type granites from the NQT). Those features all suggest insignificant crustal contamination during the magma generation.

As mentioned above, most of the lamprophyre samples have comparatively high MgO contents (8.80–9.43 wt%), Mg no. values (> 64) and Cr (> 400 ppm), with low FeOt/MgO ratios (< 1), which are consistent with the features of the primitive magmas (Tatsumi & Eggins, 1995). However, compared with the primitive

magmas, one sample JL01-2 has slightly lower MgO (8.26 wt%), Mg no. (62) and Cr (404 ppm), and higher FeOt/MgO ratios (1.08), indicating that it might have undergone a low degree of magma differentiation. In this study, we use multiple binary diagrams defining Mg no. as the abscissa to trace magma differentiation. On the binary diagrams (Fig. 7), the samples show roughly decreasing positive correlations among Cr, Ni and Mg no. values, indicating the fractionation crystallization of olivine and/or clinopyroxene. Sc/Y ratios are usually controlled by clinopyroxene crystallization, and are not influenced by the fractionation of olivine and plagioclase (Naumann & Geist, 1999). The constant Sc/Y ratios with decreasing Mg no. values therefore preclude the clinopyroxene crystallization. There is a negative correlation between CaO/ Al_2O_3 ratios and Mg no. values, further suggesting that olivine is probably the dominant fractionating mineral phase. Moreover, plagioclase, Fe–Ti oxide and apatite did not play a vital role during the magma evolution, as shown by the nearly constant Eu/Eu^* , FeOt, TiO_2 and P_2O_5 with decreasing Mg no. values.

In summary, the lamprophyre dykes could not have experienced any significant crustal contamination, but underwent a somewhat low degree of olivine crystallization.

5.c. A subduction-modified lithospheric mantle

All of the lamprophyre samples exhibit typical crustal fingerprints (e.g. obvious enrichments in Th and LREEs, and strong depletions of Nb, Ta, Ti and P; Fig. 5), and are plotted above the MORB and ocean-island basalt (OIB) mantle array on the diagram of Th/Yb versus Nb/Yb (Fig. 8), suggesting the participation of crustal materials in the magma generation.

Many studies have demonstrated that crustal contamination and the mantle metasomatism by subduction components were

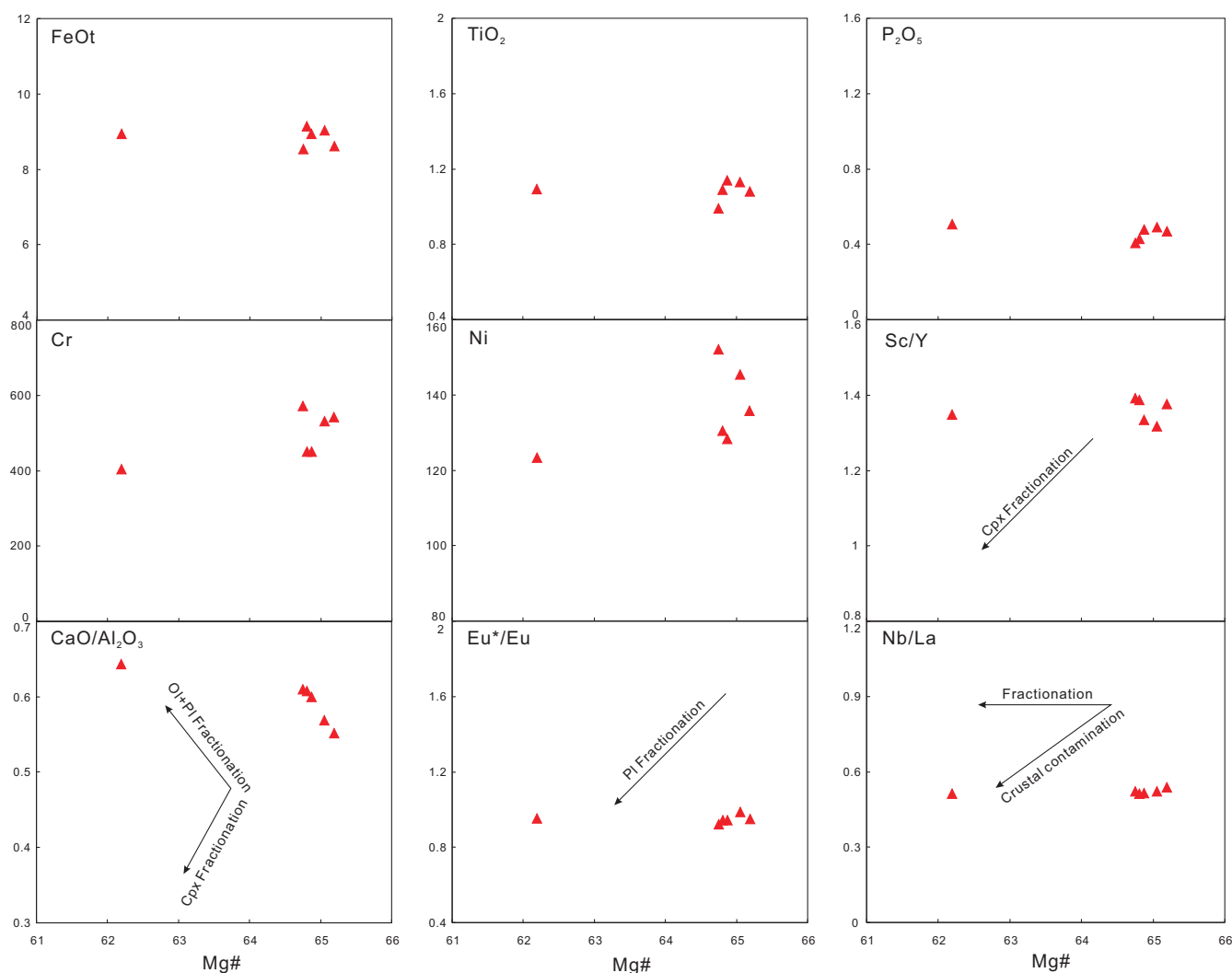


Fig. 7. (Colour online) Plots of FeOt, TiO₂, P₂O₅, Cr, Ni, Sc/Y, CaO/Al₂O₃, Eu/Eu* and Nb/La versus Mg no. for the Triassic lamprophyre dykes.

two dominating pathways for transporting the crustal components into the mafic magmas (e.g. Abdelfadil *et al.* 2013; Zhao *et al.* 2013). Because the lamprophyre dykes had experienced a negligible crustal contamination as discussed above, the mantle metasomatism by subduction components before the partial melting could be the dominant mechanism and the crustal-like compositions might be derived from the deep mantle source. The geochemical compositions of the lamprophyre samples (such as their trace-element patterns, ratios of Th/Yb and Nb/Yb) are similar to those of primitive mafic melts of the subduction-modified lithosphere in the Antarctic Peninsula (Fig. 8; Leat *et al.* 2002), further supporting a sub-arc lithospheric mantle. The lamprophyre samples have relatively high La/Nb ratios (1.86–1.95) and low La/Ba ratios (0.03–0.04), which are typically associated with a subduction-modified lithospheric mantle (Fig. 8; Saunders *et al.* 1992). Also, all have low ratios of Nb/U (3.04–3.58) and Ce/Pb (3.46–8.39) with high ratios of Zr/Nb (9.45–10.27), which are markedly distinct from those of global OIB and MORB (Sun & McDonough, 1989). Moreover, they have negative $\epsilon_{\text{Nd}}(t)$ values and relatively high $(^{87}\text{Sr}/^{86}\text{Sr})_i$ ratios. These features strongly indicate an enriched lithospheric mantle modified by subduction-related components.

Questions remain as to which subduction-related components (e.g. slab- and sediment-derived melts or fluids) participate in the lithospheric mantle source. The slab–mantle interactions usually produce mafic melts with high concentrations of TiO₂ and P₂O₅, and positive Nb and Ti anomalies relative to the primitive mantle (Sajona *et al.* 2000; Wang *et al.* 2003). The lamprophyre samples have relatively low TiO₂ and P₂O₅, and show distinctly negative Nb and Ti anomalies compared to the primitive mantle, thus excluding the contribution of the slab melt. Nb, Th and REEs are immobile in the low-temperature fluids, while Ba is mobile in the fluids and more soluble than the REEs. Several characteristic trace-elements ratios (e.g. Th/Nb, Th/Yb, Ba/La, Ba/Th) are therefore applied to reveal the influence of aqueous fluids and sediment-derived melts (Woodhead *et al.* 2001; Hanyu *et al.* 2006). All the samples have relatively constant ratios of Th/Nb and Th/Yb, and variable ratios of Ba/Th and Ba/La (Fig. 5), suggesting the addition of aqueous fluids rather than the sediment-derived melts.

5.d. Melting of a phlogopite- and spinel-bearing peridotite

Many previous studies have documented that some non-peridotite lithologies involving pyroxenite or hornblendites in the

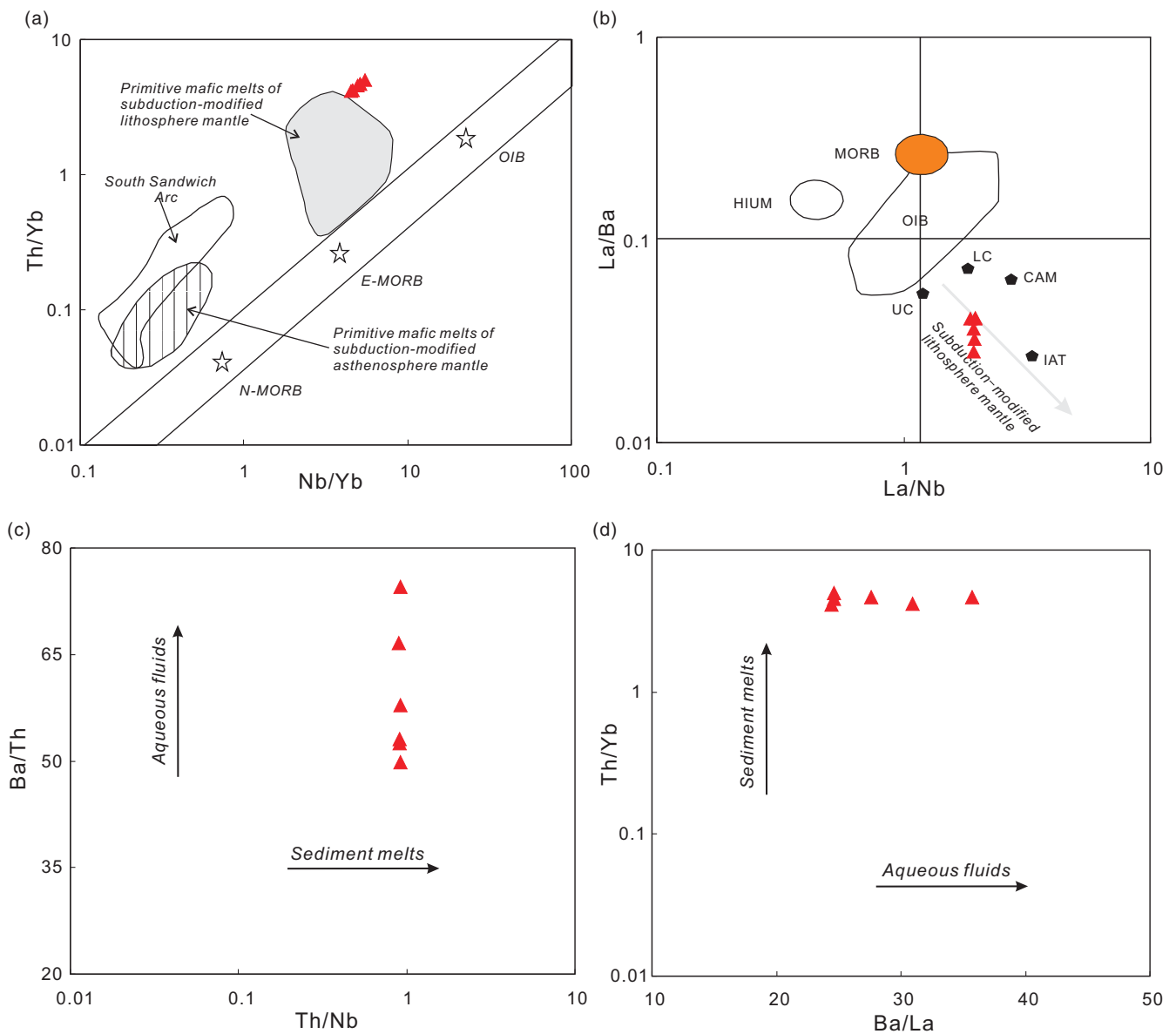


Fig. 8. (Colour online) Plots of (a) Th/Yb versus Nb/Yb (Pearce, 2014), (b) La/Ba versus La/Nb (Saunders *et al.* 1992), (c) Ba/Th versus Th/Nb and (d) Th/Yb versus Ba/La diagrams for the Triassic lamprophyre dykes.

lithospheric mantle could serve as sources of the mafic melts (Pilet *et al.* 2011; Murray *et al.* 2015). Evaluating the lithologies of the mantle source is therefore very crucial. Zn/Fe_t ratios have been widely applied to analyse the petrological features of the mantle source (Le Roux *et al.* 2010; Liu *et al.* 2020; Murray *et al.* 2015), because they are usually unaffected by the olivine crystallization, but they could be changed by the clinopyroxene or garnet crystallization. In general, pyroxenite-derived melts have higher Zn/Fe_t ratios than those of the peridotite-derived melts. All the lamprophyre samples have comparatively lower Zn/Fe_t ratios (10.98–12.29) than those of typical melts arise from partial melting of the pyroxenites (13–20), suggesting that their mantle sources are dominated by the peridotites rather than the pyroxenites.

As described above, the lamprophyre samples have relatively high K₂O contents of 1.30–1.82, and exhibit strong enrichment of LILEs (e.g. Rb, Sr; Table 2), indicating a LILE-enriched lithospheric mantle source. It has been proposed that LILEs usually

prefer to gather in volatile-bearing minerals such as amphibole and phlogopite. Melts in equilibrium with phlogopites exhibit relatively low Ba contents and Ba/Rb ratios, while melts in equilibrium with amphiboles show extremely low Rb/Sr ratios and high Ba/Rb ratios (Furman & Graham, 1999). The lamprophyre samples have relatively low Ba contents (480.4–656.4 ppm) and Ba/Rb ratios (6.19–10.62), and high Rb/Sr ratios (0.11–0.18), suggesting a phlogopite-bearing peridotite mantle (Fig. 9). Moreover, the existence of phlogopites also indicates that the hydrous fluid metasomatism appeared before the mantle melting. The samples possess relatively low ratios of Ce/Y and (Tb/Yb)_N (1.77–1.95 and 1.27–1.45, respectively), suggesting a spinel stability field (McKenzie & Bickle, 1988; Wang *et al.* 2002). Moreover, melts sourced from a garnet-bearing mantle usually show significantly higher Dy/Yb ratios (> 2.5) than those of melts derived from a spinel-bearing mantle (< 1.5; Duggen *et al.* 2005). All the samples have relatively low Dy/Yb ratios of 1.76–1.97 and plot near the

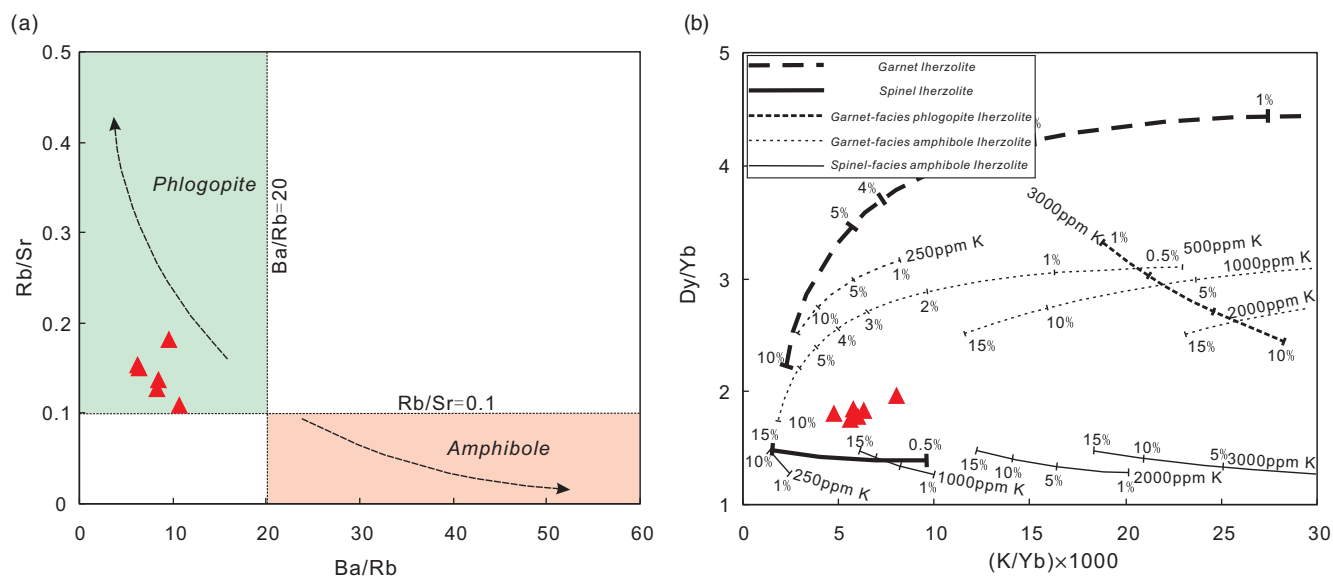


Fig. 9. (Colour online) Plots of (a) Rb/Sr versus Ba/Rb (Ma *et al.* 2014) and (b) Dy/Yb versus (K/Yb) × 1000 for the Triassic lamprophyre dykes. Melting curves in (b) after Duggen *et al.* (2005).

spinel peridotite melting curves, further implying that the lamprophyre dykes originated from partial melting of a phlogopite- and spinel-bearing peridotite mantle.

5.e. Geodynamic relationships with the Palaeo-Tethyan Ocean

Previous studies on the granitoid rocks and intermediate to acid volcanic rocks had led to the proposal of two competing mechanisms, namely the collision-related model and the subduction-related model, during the generation of the Late Triassic magmatism (Zhang *et al.* 2007, 2014; Peng *et al.* 2015; Liu *et al.* 2016a; Yang *et al.* 2020). The collision-related model refers to crustal thickening, lithospheric delamination and slab break-off (Zhang *et al.* 2007; Yuan *et al.* 2010; Peng *et al.* 2015), while the subduction-related model involves an unproven Palaeo-Tethyan oceanic subduction (Zhao *et al.* 2014, 2015; Liu *et al.* 2016a; Yang *et al.* 2020).

As mentioned above, most of the lamprophyre samples in this study have geochemical compositions similar to those of the primitive magmas (Tatsumi & Eggins, 1995), although some of them have experienced a slightly low degree of the olivine crystallization. Those lamprophyres could therefore provide new insights into the geodynamic mechanism of the Late Triassic magmatism. The lamprophyre samples have subduction-related geochemical compositions, for instance, enrichments in Th and LREEs with depletions of Nb, Ta, Ti and P, relative to the primitive mantle (Fig. 5b). Moreover, they show similar patterns and ratios of trace elements to those of the primitive melts of subduction-modified lithospheric mantle in the Antarctic Peninsula (Figs 5, 8; Leat *et al.* 2002). All of the samples have low TiO₂ contents, comparable to those of calc-alkaline basalts, and plot in the field of island-arc calc-alkaline basalts in the various tectonic discrimination diagrams by using immobile trace elements (such as DF2 versus DF1 and Hf/3-Th-Ta; Fig. 10). Such geochemical features strongly suggest a slab subduction environment. Furthermore, the collision-related model proposed that the Palaeo-Tethyan ocean might have closed during Middle Triassic time, and the generation of Triassic magmatism

could be attributed to the crustal thickening and lithospheric delamination (Zhang *et al.* 2007; Yuan *et al.* 2010; Peng *et al.* 2015). However, the identification of Middle–Upper Triassic submarine fan and deep-marine facies rocks developed in the HBSG region (Ding *et al.* 2013) and in the palaeomagnetic studies of the Upper Triassic volcanic rocks (Song *et al.* 2015) suggest that the ocean did not close during Middle Triassic time. ⁴⁰Ar–³⁹Ar geochronological results of metamorphic minerals (such as biotite and muscovite) in the deformed Triassic plutons indicate that the timing of the continental collision might be 193–201 Ma (Yang *et al.* 2012; Zhang *et al.* 2013), which is distinctly younger than the crystallization age of the lamprophyre dykes in this study (c. 216 Ma). A slab subduction might therefore have occurred during Late Triassic time.

A Triassic ocean in the central Tibetan Plateau is indicated by the voluminous Triassic ophiolitic mélanges with ages in the range 232–240 Ma (Duan *et al.* 2009; Liu *et al.* 2016b) in the western segment of the Garzê–Litang suture zone. The S-wards subduction of the Triassic ocean triggered the formation of abundant arc-like volcanic rocks, high-Mg diorites and granitoids, with ages ranging over 208–230 Ma (Zhang *et al.* 2013; Zhao *et al.* 2014, 2015; Liu *et al.* 2016a; Yang *et al.* 2020). However, a back-arc extension could be also precluded, due to the scarcity of typical back-arc basin magmatism (e.g. back-arc basin basalts) and the associated Late Triassic hydrothermal sedimentation. Adakites with ages of c. 220 Ma have been investigated in the north margin of the NQT and their generation had been considered to be inherited from partial melting of a young subducted oceanic crust (Wang *et al.* 2008). Because slab melting to produce the adakitic melts usually requires a relatively young oceanic slab subducted at depths of 70–85 km (Kepezhinskas *et al.* 1996; Wang *et al.* 2008), the eclogitization of the oceanic crust would have to have begun no later than 220 Ma. In that case, the massive eclogitization would signally increase the density of oceanic crust, and then induce the rollback of the subducted slab.

Because the mafic dykes are usually formed in a crustal extension tectonic setting, a slab rollback could induce the generation of the Late Triassic lamprophyre dykes in the central Tibetan Plateau.

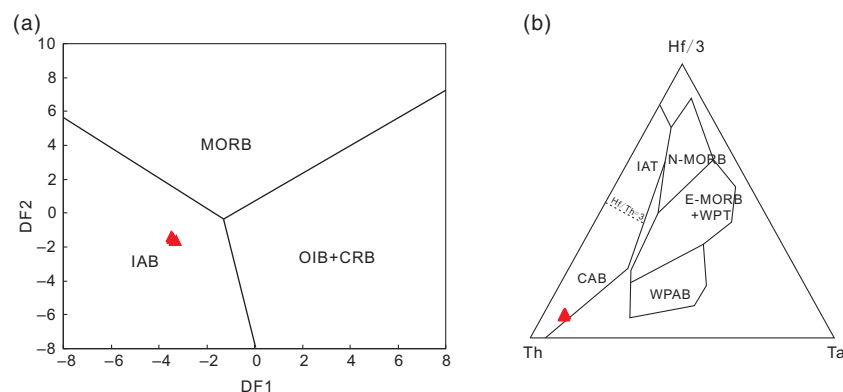


Fig. 10. (Colour online) Plots of (a) DF2 versus DF1 (Agrawal et al. 2008) and (b) (Hf/3)–Th–Ta (Wood, 1980) for the Triassic lamprophyre dykes, where DF1 and DF2 are defined as $0.3518 \ln(\text{La}/\text{Th}) + 0.6013 \ln(\text{Sm}/\text{Th}) - 1.3450 \ln(\text{Yb}/\text{Th}) + 2.1056 \ln(\text{Nb}/\text{Th}) - 5.4763$ and $-0.3050 \ln(\text{La}/\text{Th}) - 1.1801 \ln(\text{Sm}/\text{Th}) + 1.6189 \ln(\text{Yb}/\text{Th}) + 1.2260 \ln(\text{Nb}/\text{Th}) - 0.9944$, respectively. IAB – island-arc basalt; MORB – mid-ocean-ridge basalt; OIB – ocean-island basalt; CRB – continental-rift basalt; CAB – calc-alkaline basalts; IAT – island-arc tholeiites; N-MORB – normal-type MORB; E-MORB – enriched-type MORB; WPT – within-plate tholeiites; WPAB – within-plate alkaline basalts.

6. Conclusions

1. Relatively primitive lamprophyre dykes have been identified in the North Qiangtang, central Tibetan Plateau, yielding zircon U–Pb ages of 214–218 Ma with a weighted mean age of 216 ± 1 Ma.
2. The lamprophyre dykes originated from the partial melting of a phlogopite- and spinel-bearing peridotite mantle modified by subduction-related aqueous fluids, and have experienced a slightly low degree of olivine crystallization.
3. A slab subduction might have occurred during Late Triassic time, and the rollback of the oceanic lithosphere induced the lamprophyre magmatism in the central Tibetan Plateau.

Supplementary material. For supplementary material accompanying this paper visit <https://doi.org/10.1017/S001675682100100X>

Acknowledgements. This study benefited from the financial support of the National Natural Science Foundation of China (grant no. 42130309 and 41502050), the China Geological Survey (grant nos DD20160022 and 12120115026901), the Foundation of the State Key Laboratory of Petroleum Resources and Prospecting, China University of Petroleum, Beijing (PRP/open-1908), the Open Foundation of Top Disciplines in Yangtze University (grant no. 2019KFJJ0818017), and the Yangtze Youth Fund (grant no. 2015cqn29). We thank Zhao-Chu Hu, Lian Zhou, Lu Chen and Hong-Fang Chen for their help with analytical work.

Conflicts of interest. None.

References

- Abdelfadil KM, Romer RL, Seifert T and Lobst R (2013) Calc-alkaline lamprophyres from Lusatia (Germany)—Evidence for a repeatedly enriched mantle source. *Chemical Geology* **353**, 230–45.
- Aghazadeh M, Prelević D, Badrzadeh Z, Braschi E, van den Bogaard P and Coticelli S (2015) Geochemistry, Sr–Nd–Pb isotopes and geochronology of amphibole- and mica-bearing lamprophyres in northwestern Iran: Implications for mantle wedge heterogeneity in a palaeo-subduction zone. *Lithos* **216–217**, 352–69.
- Agrawal S, Guevara M and Verma SP (2008) Tectonic discrimination of basic and ultrabasic volcanic rocks through log-transformed ratios of immobile trace elements. *International Geology Review* **50**, 1057–79.
- Dan W, Wang Q, White WM, Zhang X, Tang G, Jiang Z, Hao L and Ou Q (2018) Rapid formation of eclogites during a nearly closed ocean: revisiting the Pianshishan eclogite in Qiangtang, central Tibetan Plateau. *Chemical Geology* **477**, 112–22.
- DePaolo DJ (1981) Trace element and isotopic effects of combined wallrock assimilation and fractional crystallization. *Earth and Planetary Science Letters* **53**, 189–202.
- Ding L, Yang D, Cai FL, Pullen A, Kapp P, Gehrels GE, Zhang LY, Zhang QH, Lai QZ, Yue YH and Shi RD (2013) Provenance analysis of the Mesozoic Hoh-Xil-Songpan-Ganzi turbidites in northern Tibet: implications for the tectonic evolution of the eastern Paleo-Tethys Ocean. *Tectonics* **32**, 34–48.
- Duan QF, Wang JX, Bai YS, Yao HZ, He LQ, Zhang KX, Kou XH and Li J (2009) Zircon SHRIMP U–Pb dating and litho-geochemistry of gabbro from the ophiolite in southern Qinghai Province. *Geology in China* **36**, 291–99.
- Duggen S, Hoernle K, Van Den Bogaard P and Garbe-Schönberg D (2005) Post-collisional transition from subduction- to intraplate-type magmatism in the westernmost Mediterranean: evidence for continental-edge delamination of subcontinental lithosphere. *Journal of Petrology* **46**, 1155–201.
- Furman T and Graham D (1999) Erosion of lithospheric mantle beneath the East African Rift system: geochemical evidence from the Kivu volcanic province. *Lithos* **48**, 237–62.
- Gao S, Rudnick RL, Yuan HL, Liu XM, Liu YS, Xu WL, Ayers J, Wang XC and Wang QH (2004) Recycling lower continental crust in the North China craton. *Nature* **432**, 892–7.
- Halama R, Marks M, Brüggemann G, Siebel W, Wenzel T and Markl G (2004) Crustal contamination of mafic magmas: evidence from a petrological, geochemical and Sr–Nd–Os–O isotopic study of the Proterozoic Isortoq dike swarm, South Greenland. *Lithos* **74**, 199–232.
- Hanyu T, Tatsumi Y, Nakai S, Chang Q, Miyazaki T, Sato K, Tani K, Shibata T and Yoshida T (2006) Contribution of slab melting and slab dehydration to magmatism in the NE Japan arc for the last 25 Myr: Constraints from geochemistry. *Geochemistry, Geophysics, Geosystems* **7**, <https://doi.org/10.1029/2005GC001220>.
- He SP, Li RS, Wang C, Gu PY, Yu PS, Shi C and Cha XF (2013) Research on the formation age of the Ningduo rock group in Chandu block: Evidence for the existence of basement in the North Qiangtang. *Earth Science Frontiers* **20**, 15–24.
- He S, Li R, Wang C, Zhang H, Ji W, Yu P, Gu P and Shi C (2011) Discovery of ~4.0 Ga detrital zircons in the Changdu Block, North Qiangtang, Tibetan Plateau. *Chinese Science Bulletin* **56**, 647–58.
- Kapp P, Yin A, Manning CE, Harrison TM, Taylor MH and Ding L (2003) Tectonic evolution of the early Mesozoic blueschist-bearing Qiangtang metamorphic belt, central Tibet. *Tectonics* **22**, 17.1–17.22.
- Karsli O, Dokuz A, Kaliwoda M, Uysal I, Aydin F, Kandemir R and Fehr K (2014) Geochemical fingerprints of Late Triassic calc-alkaline lamprophyres from the Eastern Pontides, NE Turkey: A key to understanding lamprophyre formation in a subduction-related environment. *Lithos* **196–197**, 181–97.
- Kepezhinskas P, Defant MJ and Drummond MS (1996) Progressive enrichment of island arc mantle by melt-peridotite interaction inferred from Kamchatka xenoliths. *Geochimica et Cosmochimica Acta* **60**, 1217–29.
- Le Roux V, Lee CTA and Turner SJ (2010) Zn/Fe systematics in mafic and ultramafic systems: implications for detecting major element heterogeneities in the Earth's mantle. *Geochimica et Cosmochimica Acta* **74**, 2779–96.
- Leat PT, Riley TR, Wareham CD, Millar IL, Kelley SP and Storey BC (2002) Tectonic setting of primitive magmas in volcanic arcs: an example from the Antarctic Peninsula. *Journal of the Geological Society* **159**, 31–44.
- Li C, Zhai QG, Dong YP, Zeng QG and Huang XP (2007) Longmu Co-Shuanghu plate suture and evolution records of paleo-Tethyan oceanic in

- Qiangtang area, Qinghai-Tibet plateau. *Frontiers in Earth Science China* **1**, 257–64.
- Liu B, Ma CQ, Huang J, Xiong FH, Zhang X and Guo YH** (2016a) Petrogenetic mechanism and tectonic significance of Triassic Yushu volcanic rocks in the northern part of the North Qiangtang Terrane. *Acta Petrologica et Mineralogica* **35**, 1–15.
- Liu B, Ma C, Guo Y, Xiong F, Guo P and Zhang X** (2016b) Petrogenesis and tectonic implications of Triassic mafic complexes with MORB/OIB affinities from the western Garzê-Litang ophiolitic mélange, central Tibetan Plateau. *Lithos* **260**, 253–67.
- Liu B, Xu Y, Li Q, Sun Y, Zhao S Q, Huang J, Dong H and Rong Y** (2020) Origin of Triassic mafic magmatism in the North Qiangtang terrane, central Tibetan Plateau: implications for the development of a continental back-arc basin. *Journal of the Geological Society* **177**, 826–42.
- Liu Y, Gao S, Hu Z, Gao C, Zong K and Wang D** (2010) Continental and Oceanic crust recycling-induced melt-peridotite interactions in the trans-North China Orogen: U-Pb dating, Hf isotopes and trace elements in Zircons from Mantle Xenoliths. *Journal of Petrology* **51**, 537–71.
- Liu Y, Tan J, Wei J, Zhao S, Liu X, Gan J and Wang Z** (2019) Sources and petrogenesis of Late Triassic Zhiduo volcanics in the northeast Tibet: Implications for tectonic evolution of the western Jinsha Paleo-Tethys Ocean. *Lithos* **336–337**, 169–82.
- Liu YS, Hu ZC, Gao S, Günther D, Xu J, Gao CG and Chen HH** (2008) In situ analysis of major and trace elements of anhydrous minerals by LA-ICP-MS without applying an internal standard. *Chemical Geology* **257**, 34–43.
- Ma L, Jiang S, Hou M, Dai B, Jiang Y, Yang T, Zhao K, Pu W, Zhu Z and Xu B** (2014) Geochemistry of Early Cretaceous calc-alkaline lamprophyres in the Jiaodong Peninsula: implication for lithospheric evolution of the eastern North China Craton. *Gondwana Research* **25**, 859–72.
- McKenzie D and Bickle MJ** (1988) The volume and composition of melt generated by extension of the lithosphere. *Journal of Petrology* **29**, 625–79.
- Metcalfe I** (2013) Gondwana dispersion and Asian accretion: tectonic and palaeogeographic evolution of eastern Tethys. *Journal of Asian Earth Sciences* **66**, 1–33.
- Mullen EK, Weis D, Marsh NB and Martindale M** (2017) Primitive arc magma diversity: new geochemical insights in the Cascade Arc. *Chemical Geology* **448**, 43–70.
- Murray K, Ducea MN and Schoenbohm L** (2015) Foundering-driven lithospheric melting: the source of central Andean mafic lavas on the Puna Plateau (22°S–27°S). *Geological Society of America, Memoirs* **212**, 139–66.
- Naumann TR and Geist DJ** (1999) Generation of alkalic basalt by crystal fractionation of tholeiitic magma. *Geology* **27**, 423.
- Pearce JA** (1982) Trace element characteristics of lavas from destructive plate boundaries. In *Andesites: Orogenic Andesites and Related Rocks* (ed RS Thorpe), pp. 525–48. Chichester: John Wiley and Sons.
- Pearce JA** (2014) Immobile element fingerprinting of ophiolites. *Elements* **10**, 101–8.
- Peng T, Zhao G, Fan W, Peng B and Mao Y** (2015) Late Triassic granitic magmatism in the Eastern Qiangtang, Eastern Tibetan Plateau: Geochronology, petrogenesis and implications for the tectonic evolution of the Paleo-Tethys. *Gondwana Research* **27**, 1494–508.
- Pilet S, Baker MB, Müntener O and Stolper EM** (2011) Monte Carlo simulations of metasomatic enrichment in the lithosphere and implications for the source of alkaline basalts. *Journal of Petrology* **52**, 1415–42.
- Polat A and Hofmann AW** (2003) Alteration and geochemical patterns in the 3.7–3.8 Ga Isua greenstone belt, West Greenland. *Precambrian Research* **126**, 197–218.
- Pullen A, Kapp P, Gehrels GE, Vervoort JD and Ding L** (2008) Triassic continental subduction in central Tibet and Mediterranean-style closure of the Paleo-Tethys Ocean. *Geology* **36**, 351–4.
- Rock NMS** (1991) *Lamprophyres*. London: Blackie and Son Ltd., Glasgow.
- Rogers G and Hawkesworth CJ** (1989) A geochemical traverse across the North Chilean Andes: evidence for crust generation from the mantle wedge. *Earth and Planetary Science Letters* **91**, 271–85.
- Sajona FG, Maury RC, Pubellier M, Leterrier J, Bellon H and Cotten J** (2000) Magmatic source enrichment by slab-derived melts in a young post-collision setting, central Mindanao (Philippines). *Lithos* **54**, 173–206.
- Saunders AD, Storey M, Kent RW and Norry MJ** (1992) Consequences of plume-lithosphere interactions. In *Magmatism and the Causes of Continental Break-up* (eds BC Storey, T Alabaster and RJ Pankhurst), pp. 41–60. Geological Society of London, Special Publication no. 68.
- Song P, Ding L, Li Z, Lippert PC, Yang T, Zhao X, Fu J and Yue Y** (2015) Late Triassic paleolatitude of the Qiangtang block: implications for the closure of the Paleo-Tethys Ocean. *Earth and Planetary Science Letters* **424**, 69–83.
- Sun SS and McDonough WF** (1989) Chemical and isotopic systematics of oceanic basalts: implications for mantle composition and processes. In *Magmatism in the Ocean Basins* (eds AD Saunders and MJ Norry), pp. 313–45. Geological Society of London, Special Publication no. 42.
- Tan J, Wei J, Zhao S, Li Y, Liu Y, Liu X, Zhang F, Gan J and Wang Z** (2019) Petrogenesis of Late Triassic high-Mg diorites and associated granitoids with implications for Paleo-Tethys evolution in the northeast Tibetan Plateau. *GSA Bulletin* **132**, 955–76.
- Tao Y, Bi X, Li C, Hu R, Li Y and Liao M** (2014) Geochronology, petrogenesis and tectonic significance of the Jitang granitic pluton in eastern Tibet, SW China. *Lithos* **184–187**, 314–23.
- Tatsumi Y and Eggins S** (1995) *Subduction Zone Magmatism*. Cambridge: Blackwell Science.
- Taylor SR and McLennan SM** (1985) *The Continental Crust: Its Composition and Evolution*. Oxford: Blackwell Scientific Publications.
- Wang H, Wu Y, Qin Z, Zhu L, Liu Q, Liu X, Gao S, Wijbrans JR, Zhou L, Gong H and Yuan H** (2013) Age and geochemistry of Silurian gabbroic rocks in the Tongbai orogen, central China: Implications for the geodynamic evolution of the North Qinling arc-back-arc system. *Lithos* **179**, 1–15.
- Wang K, Plank T, Walker JD and Smith EI** (2002) A mantle melting profile across the Basin and Range, SW USA. *Journal of Geophysical Research: Solid Earth* **107**, ECV5-1–ECV5-21.
- Wang Q, Wyman DA, Xu JF, Wan YS, Li C, Zi F, Jiang Z, Qiu H, Chu Z, Zhao Z and Dong Y** (2008) Triassic Nb-enriched basalts, magnesian andesites, and adakites of the Qiangtang terrane (Central Tibet): evidence for metasomatism by slab-derived melts in the mantle wedge. *Contributions to Mineralogy and Petrology* **155**, 473–90.
- Wang Q, Zhao ZH, Bai ZH, Bao ZW, Xiong XL, Mei HJ, Xu JF and Wang YX** (2003) Carboniferous adakites and Nb-enriched arc basaltic rocks association in the Alataw Mountains, north Xinjiang: interactions between slab melt and mantle peridotite and implications for crustal growth. *Chinese Science Bulletin* **48**, 2108–15.
- Winchester JA and Floyd PA** (1977) Geochemical discrimination of different magma series and their differentiation products using immobile elements. *Chemical Geology* **20**, 325–43.
- Wood DA** (1980) The application of a Th-Hf-Ta diagram to problems of tectonomagmatic classification and to establishing the nature of crustal contamination of basaltic lavas of the British Tertiary volcanic Province. *Earth and Planetary Science Letters* **50**, 11–30.
- Woodhead JD, Hergt JM, Davidson JP and Eggins SM** (2001) Hafnium isotope evidence for ‘conservative’ element mobility during subduction zone processes. *Earth and Planetary Science Letters* **192**, 331–46.
- Xu W, Liu F and Dong Y** (2020) Cambrian to Triassic geodynamic evolution of central Qiangtang, Tibet. *Earth-Science Reviews* **201**, 103083.
- Xu Z, Dilek Y, Cao H, Yang J, Robinson P, Ma C, Li H, Jolivet M, Roger F and Chen X** (2015) Paleo-Tethyan evolution of Tibet as recorded in the East Cimmerides and West Cathaysides. *Journal of Asian Earth Sciences* **105**, 320–37.
- Yan QR, Wang ZQ, Liu SW, Li QG, Zhang HY, Wang T, Liu DY, Shi YR, Jian P, Wang JG, Zhang DH and Zhao J** (2005) Opening of Tethys in southwest China and its significance to the breakup of East Gondwanaland in the late Paleozoic, evidence from SHRIMP U-Pb zircon analyses for the Garzê ophiolite block. *Chinese Science Bulletin* **50**, 158–66.
- Yang K, Liu B, Ma CQ, Sun Y, Zhang F, Mou JZ, He Y and Xiao L** (2020) Petrogenesis and geodynamic setting of Triassic pyroxene diorite-porphyrite from the North Qiangtang Terrane: geochronology, mineral petrogeochemistry and Sr-Nd-Hf isotope constraints. *Earth Science* **45**, 1490–502.
- Yang TN, Hou ZQ, Wang Y, Zhang HR and Wang ZL** (2012) Late Paleozoic to Early Mesozoic tectonic evolution of northeast Tibet: evidence from the Triassic composite western Jinsha-Garzê-Litang suture. *Tectonics* **31**, 1–20.

- Yang TN, Zhang HR, Liu YX, Wang ZL, Song YC, Yang ZS, Tian SH, Xie HQ and Hou KJ** (2011) Permo-Triassic arc magmatism in central Tibet: evidence from zircon U–Pb geochronology, Hf isotopes, rare earth elements, and bulk geochemistry. *Chemical Geology* **3–4**, 270–82.
- Yuan C, Zhou MF, Sun M, Zhao YJ, Wilde S, Long X and Yan D** (2010) Triassic granitoids in the eastern Songpan Ganzi Fold Belt, SW China: magmatic response to geodynamics of the deep lithosphere. *Earth and Planetary Science Letters* **290**, 481–92.
- Zhai QG, Zhang RY, Jahn BM, Li C, Song S and Wang J** (2011) Triassic eclogites from central Qiangtang, northern Tibet, China: petrology, geochronology and metamorphic P–T path. *Lithos* **125**, 173–89.
- Zhang HF, Parrish R, Zhang L, Xu WC, Yuan H, Gao S and Crowley QG** (2007) A-type granite and adakitic magmatism association in Songpan–Garze fold belt, eastern Tibetan Plateau: implication for lithospheric delamination. *Lithos* **97**, 323–35.
- Zhang HR, Yang TN, Hou ZQ, Song YC, Chen X F, Ding Y, Chen W and Hou KJ** (2013) Chronology and geochemistry of mylonitic quartz diorites in the Yushu melange, central Tibet. *Acta Petrologica Sinica* **29**, 3871–82.
- Zhang LY, Ding L, Pullen A, Xu Q, Liu DL, Cai F, Yue Y, Lai Q, Shi R, Ducea MN, Knapp P and Chapman A** (2014) Age and geochemistry of western Hoh-Xil–Songpan–Ganzi granitoids, northern Tibet: Implications for the Mesozoic closure of the Paleo-Tethys ocean. *Lithos* **190–191**, 328–48.
- Zhang N, Li JB, Yang YS and Na FC** (2012) Petrogeochemical characteristics and tectonic setting of the Wandaohu ophiolite melange, Jinshajiang suture, Tibet. *Acta Petrologica Sinica* **28**, 1291–304.
- Zhang Y and Zhang K** (2017) Early Permian Qiangtang flood basalts, northern Tibet, China: a mantle plume that disintegrated northern Gondwana? *Gondwana Research* **44**, 96–108.
- Zhao SQ, Fu LB, Wei JH, Tan J, Wang XC, Zhao ZX and Li X** (2015) Petrogenesis and geodynamic setting of Late Triassic quartz diorites in Zhiduo area, Qinghai province. *Earth Science–Journal of the China University of Geosciences* **40**, 61–76.
- Zhao SQ, Tan J, Wei JH, Tian N, Zhang DH, Liang SN and Chen JJ** (2014) Late Triassic Batang Group arc volcanic rocks in the northeastern margin of Qiangtang terrane, northern Tibet: partial melting of juvenile crust and implications for Paleo-Tethys ocean subduction. *International Journal of Earth Sciences* **104**, 369–87.
- Zhao Z, Dai L and Zheng Y** (2013) Postcollisional mafic igneous rocks record crust–mantle interaction during continental deep subduction. *Scientific Reports* **3**, <https://doi.org/10.1038/srep03413>.